Journal of Environmental Radioactivity 251–252 (2022) 106966

Contents lists available at ScienceDirect

Journal of Environmental Radioactivity

journal homepage: www.elsevier.com/locate/jenvrad

Quantification of ^{37}Ar emanation fractions from irradiated natural rock samples and field applications

S. Musy [a,*], P. Casolaro [b], G. Dellepiane [b], A. Berger [c], S. Braccini [b], R. Purtschert [a]

[a] Climate and Environmental Physics and Oeschger Center for Climate Change Research, University of Bern, Sidlerstrasse 5, 3012, Bern, Switzerland
[b] Albert Einstein Center for Fundamental Physics (AEC), Laboratory for High Energy Physics (LHEP), University of Bern, Sidlerstrasse 5, 3012, Bern, Switzerland
[c] Institute of Geological Sciences, University of Bern, Baltzerstrasse 1+3, 3012, Bern, Switzerland

ARTICLE INFO

Keywords:
Emanation fraction
^{37}Ar
CTBT
Irradiated rocks
Neutron activation
Medical cyclotron

ABSTRACT

Underground-produced ^{37}Ar can be used for underground nuclear explosions (UNE) detection and for groundwater dating. The quantification of the emanation, that is the fraction of activity produced in the rock that escapes to the pore space, is essential for predicting the background activity expected in natural environments. We propose an experiment in which artificial $CaCO_3$ powder and natural rock particles are irradiated with neutrons in a routinely operated medical cyclotron, whose energy spectrum is experimentally measured. The produced activity was quantified and compared with the emanated activity to determine the emanating fraction. The results showed consistent and reproducible patterns with a dominance of the recoil process at small scales (<2 mm). We observed emanation values $\leq 1\%$ with a dependency on the grain size and the inner geometry of particles. Soil weathering and the presence of water increased the recoil emanation. The atoms produced that were instantaneously recoiled in the intra- or inter-granular pore space left macroscopic samples by diffusion on timescales of days to weeks ($D_{eff} = 10^{-12} - 10^{-16}$ m^2 s^{-1}). This diffusive transport determines the activity that prevails in the fluid-filled pore space accessible for groundwater or soil gas sampling.

1. Introduction

In geoscience, isotopes produced underground are used for widespread applications like for example exposure dating [^{36}Cl, ^{10}Be (Alfimov and Ivy-Ochs, 2009; Schaller et al., 2002)], groundwater dating [^{39}Ar, ^{37}Ar, ^{4}He, ^{222}Rn (Lehmann and Purtschert, 1997; Peel et al., 2022; Schilling et al., 2017; Solomon et al., 1996)], or nuclear explosion monitoring [^{37}Ar, ^{131}Xe, ^{133}Xe (Aalseth et al., 2011; Guillon et al., 2016; Riedmann and Purtschert, 2011)]. The relationship between the number of atoms produced in the rock and the number of atoms released in the surrounding fluid phase is crucial for many of them. This so-called emanation fraction determines substantially the activities that are ultimately observed in the pore space. Emanation is commonly difficult to predict because it depends on many factors including the production mechanism, specific location of production in the grain, and rock characteristics. The release mechanisms involved include instantaneous recoil, time-dependent diffusion, and advective transport. Stable nuclides accumulate in the rock until a production-emanation equilibrium is achieved. Hence, the number of atoms produced equals the number of atoms reaching the fluid phase. In sedimentary aquifers this situation is often realized for $^{4}He_{RAD}$, which is produced in the U/Th decay chains. In contrast, for radioactive nuclides emanation is limited because part of the produced atoms decays during the emanation process (Yokochi et al., 2012).

Among isotopes produced underground, ^{37}Ar is a radioactive noble gas [$t_{1/2} = 34.95 \pm 0.08$ days, Renne and Norman (2001)] with multiple applications. For instance, ^{37}Ar is used as an indicator of clandestine underground nuclear explosions (UNE) during on-site inspections (OSI) under the Comprehensive Nuclear Test-Ban Treaty (CTBT) (Aalseth et al., 2011; Carrigan et al., 1996). It is produced in large amounts by neutron activation of calcium (reaction channel: ^{40}Ca(n,α)^{37}Ar) in the cavity melt and in the rock surrounding an UNE cavity (Haas et al., 2010). Activity concentrations in subsurface gas exceeding natural background levels can thus be interpreted as a signal of a nuclear test (Guillon et al., 2016; Riedmann and Purtschert, 2011). ^{37}Ar is also used for young groundwater dating, where its activity in water is an indicator of the depth-integrated underground water residence time (Schilling et al., 2017). This is important for river water recharge in alluvial aquifers. ^{37}Ar has potential applications as an indicator of ^{39}Ar underground production (Edmunds et al., 2014; Forster et al., 1989).

* Corresponding author.
E-mail address: stephanie.musy@unibe.ch (S. Musy).

https://doi.org/10.1016/j.jenvrad.2022.106966
Received 28 March 2022; Received in revised form 27 June 2022; Accepted 11 July 2022
Available online 5 August 2022

^{37}Ar is naturally produced in the atmosphere by cosmic-ray neutron capture on ^{40}Ar (reaction channel: ^{40}Ar(n,4n)^{37}Ar). The resulting tropospheric specific ^{37}Ar activity concentration is ~1 mBq/m$^3_{air}$ (Johnson et al., 2015; Lal and Peters, 1962; Riedmann and Purtschert, 2011). These levels are negligible compared to ^{37}Ar activities produced and released in the underground. In shallow depths (up to a few meters), ^{37}Ar is predominantly produced by the activation of calcium (Ca) by cosmogenic neutrons via the reaction ^{40}Ca(n,α)^{37}Ar (Fabryka-Martin, 1988). This leads to activity concentrations in soil air of up to 1000 mBq/m$^3_{air}$ (Riedmann and Purtschert, 2011). At greater depths, muon capture processes and reactions by muon-induced neutrons and neutrons from and U/Th decay chains become increasingly important (Heisinger et al., 2002; Spannagel and Fireman, 1972; Šrámek et al., 2017). However, the reaction ^{36}Ar(n,γ)^{37}Ar on argon dissolved in air equilibrated water is negligible in most cases: a rock with 1 wt% Ca, 20% porosity, and 1% emanation releases 300 times more ^{37}Ar than what is produced on ^{36}Ar dissolved in air saturated water.

Constraining emanation fractions in groundwater field studies or in soils is problematic because of the difficulty in distinguishing between production and transport mechanisms. Radioargon emanation fractions of 0.1–20% have been previously estimated in field scale studies (Andrews et al., 1991; Krishnaswami and Seidemann, 1988; Lehmann and Purtschert, 1997; Loosli et al., 1989; Pearson et al., 1991). ^{40}Ar/^{39}Ar rock dating studies reached similar conclusions (Jourdan et al., 2007; Onstott et al., 1995; Paine et al., 2006). Alternatively, emanation fractions can be determined under laboratory conditions, where soil samples are stored in closed chambers in which the activity builds up over time (Chau et al., 2005). An intrinsic complication is poor knowledge of the energy-dependent production cross-section, especially for thermal and epithermal neutrons. Few irradiation experiments have been performed to constrain the thermal production cross section (Forster et al., 1989; Wilson and Biegalski, 2015). Johnson et al. (2021, 2018) suggested an experimental setup to determine the ^{37}Ar emanation fractions. However, a systematic assessment of ^{37}Ar emanation in natural samples of various sizes and a broadening of the concepts to real aquifer cases are, to our knowledge, still lacking in the literature. Many experimental and numerical emanation studies have been conducted on radon (^{222}Rn). In particular, Sakoda and Ishimori (2017) presents a detailed review of the state-of-the-art in this domain, whose concepts can be applied to other isotopes, including ^{37}Ar.

Herein, we present an experiment in which natural samples are exposed to a low-intensity neutron field available at the medical cyclotron facility at the Bern University Hospital [Inselspital; (Braccini, 2016)]. Neutrons are produced using a (p,n) reaction and the neutron spectrum was measured using a novel neutron spectrometer, DIAMON (Pola et al., 2020). The emanated ^{37}Ar atoms were extracted, and their activity was measured in gas-proportional counters. The produced ^{37}Ar activity was calculated and the emanation fractions of (i) pure calcite powder, (ii) unconsolidated aquifer sediment powder, (iii) various size fractions of sieved aquifer material, (iv) aquifer pebbles, and (v) limestone fragments were determined as the ratio between the activity measured and the activity produced. A conceptual model of emanation in porous aquifers, describing a two-step process consisting of instantaneous recoil followed by time dependent diffusion, is proposed. The factors controlling recoil emanation, such as grain size, target element distribution, weathering, and the presence of water, are discussed based on our results. The importance of diffusion in the solid phase at various temperatures was assessed and further constrained using a heating experiment. Finally, the relevance of the diffusion processes in the pore space of macroscopic samples was examined using a simplified spherical grain model.

2. Methods

2.1. Experiment

2.1.1. Sample description and treatment

Five different groups of samples were investigated:

Group (i): As a simple model and reference material, ultrapure calcium carbonate powder [calcite (=$CaCO_3$); >99.95% purity, Sigma-Aldrich-398101] was used to determine the production of Ca^{2+} with limited structural effects or interfering reactions. This powder has a homogeneous mineralogy of pure calcite, which results in 40 wt% calcium, and an average particle size of 17 ± 7 μm (determined by measurements on representative 30–50 grains in a light microscope). ^{37}Ar temperature-dependent emanation from this material was further investigated in a heating experiment (Section 4.4).

Group (ii): Natural soil and sediment samples were collected from a drill core (P-54, Table 1) in Emmental, an alluvial valley in west-central Switzerland. This aquifer is composed of Pleistocene glaciofluvial sediments: sandy gravels and cobbles, with a variable proportion of silts (Käser and Hunkeler, 2016; Schilling et al., 2017). The core was 8 m long and subdivided into 1 m sections. Each depth interval was mixed and sampled to assess its chemical composition. At "Activation Laboratories" (in Ontario, Canada), the samples were first dried at 105 °C for several hours, pulverized, and fused with lithium metaborate/tetraborate before being digested in a weak nitric acid solution. The elemental composition was then analyzed by ICP-MS (Table A-1 in Appendix A; Actlabs, 2020). The proportion of calcium was stoichiometrically derived from the oxide form (CaO, Table 1). The average grain size of the powdered sediment samples was 1.9 ± 0.8 μm.

Group (iii): Sections ranging from 1 to 3 m of the above-described drill core were merged, mixed, and sieved into five different particle size categories (Fig. 1). The chemical composition of the merged sample P54–B is the average of the intervals P54-2 and P54-3.

Group (iv): Two solid-rock pebbles were collected from the drill core of borehole P54. After being cleaned with fresh water, the samples were dried for several hours at room temperature. After irradiation, petrographic thin sections were prepared for the structural analyses. The remainder of the samples were pulverized to determine their chemical composition. The first used pebble was a gneiss consisting mainly of quartz, albite, white mica, and chlorite with a micrometer-scale porosity of <1% which was visually estimated from the SEM images (Fig. B-1 in Appendix B). Calcium was less abundant (<1 wt%) than potassium (approximately 2 wt%). The second used pebble was siliceous limestone consisting of ~65 wt% calcite, ~35 wt% quartz, and accessory iron oxides (e.g., hematite and/or magnetite). Its porosity was also approximately <1%.

Group (v): The last type of sample was fragments of Cretaceous limestone (so-called "Pierre jaune de Neuchâtel" from the Hauterivian stage) collected from the Swiss Jura Massif (Strasser et al., 2016). This formation has a porosity of 8–19% (Rousset, 2006) and contains an average 33.7 (±0.8) wt% Ca (Table 1). Two batches of 4–5 small samples were dried for 24 h at 110 °C in a vacuum oven before being weighted. Half of the rock fragments were soaked in degassed water for more than 72 h. With the use of degassed water, interfering reactions on dissolved ^{36}Ar are minimized. The pore water saturation in the "dry" sample is assumed to be 0%, resp. > 50% in the "wet" sample. This was determined by the wet-dry mass difference and a total porosity of 12%.

2.1.2. Irradiation containers and conditions

An important criterion for the selection of suitable irradiation containers is a material featuring a low cross-section for neutron capture and neutron scattering. $CaCO_3$ powder samples were irradiated in tubes made of pure silica quartz (Heraeus Heralux®) with a diameter of 8 mm and a volume of ~10 cm^3 (Fig. 2A). Special attention was paid to avoid borosilicate materials because of the high absorption cross-section of boron for thermal neutrons. After loading the tubes with the sample

Table 1
Irradiated samples grouped in relation to sample origin and purpose of the irradiation experiment. The given depth ranges refer to merged drill-core intervals. The calcium content was calculated from the CaO content (Table A-1 in Appendix). The samples P54-1 to P54-8, as well as P54–B, refer to the Pleistocene glaciofluvial material from a drill-core in the Emmental Valley in Switzerland.

	Sample	Depth Range	Type	Irradiated mass [G]	Particle size[a]	CA [WT%]	Purpose
GROUP (I)	$CaCO_3$		Powder	2.7	17 (±7) μm	40	Production mass dependency (20 °C)
				5			
				8			
				5.1			Heated for 8 h at 200 °C
				5			Heated for 8 h at 500 °C
				5.1			Heated for 8 h at 800 °C
GROUP (II)	P54-1	0–1 m	Powder	50	1.9 (±0.8) μm	5.8	Recoil emanation assessment
	P54-2	1–2 m		7.59		9.0	
	P54-3	2–3 m		7.66		11.5	
	P54-4	3–4 m		50.8		12.1	
	P54-5	4–5 m		7.39		13.4	
	P54-8	7–8 m		51.1		19	
GROUP (III)	P54–B	1–3 m	Sieved fraction	11.3	>2 mm	10.3	Particle size emanation dependency
				16.2	2 mm–600 μm		
				11.3	600 μm–212 μm		
				12.4	212 μm–63 μm		
				11.4	<63 μm		
GROUP (IV)	Gneiss		Pebbles	31.5	3.5 × 4 × 1 cm	0.4	Emanation from undisturbed macroscopic rock fragments
	Siliceous limestone			31.32	3 × 3 × 1.5 cm	26.4	
GROUP (V)	Yellow limestone		Limestone fragments	37–39	2 × 2 × 3 cm	33.7 (±0.8)	Water emanation dependency

[a] For the pebbles, the "particle size" refers to the actual pebble size. For the limestone, the "particle size" refers to the average size of the irradiated fragments.

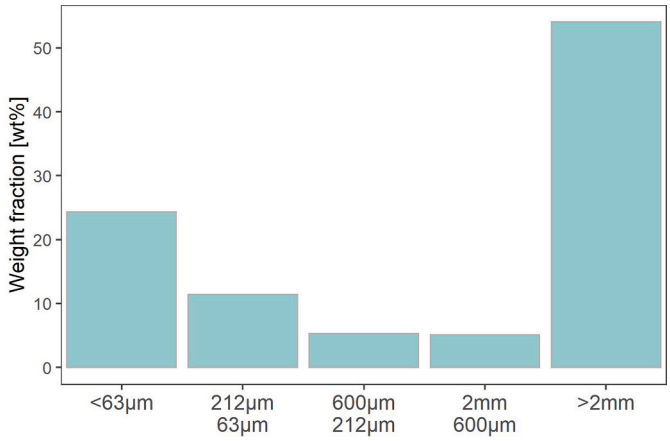

Fig. 1. Weight fraction in each particle size category for the sample P54–B. The material was first sieved through mesh apertures of 0.063, 0.212, 0.6 and 2.0 mm and weighted.

material, they were evacuated ($<10^{-2}$ mbar absolute pressure) to remove air from the pores before being fused under vacuum.

Natural samples from the drilling cores (groups ii-v) were irradiated in alloy vessels with a volume of 180 cm^3. The volume section containing the sample material was isolated using filters with a mesh of 20 μm made of sintered bronze (Pfeiffer, ZRS122ZRS040) and a stainless-steel filter with a mesh of 60 μm (Swagelok, SS-4TF-60, Fig. 2B). Powder and sieved fraction samples were placed in small nylon bags (25 μm mesh). In contrast to the quartz tubes, each container was used multiple times and carefully cleaned with alcohol and compressed air between irradiation runs to prevent cross-contamination. After loading the containers and before irradiation, they were evacuated for at least 24 h ($<10^{-2}$ mbar). In contrast, dry and wet limestone samples were irradiated in a helium matrix at ~1 bar. The sample transfer from the degassed water to the irradiation container was also performed under a helium atmosphere to prevent air contamination.

Cross-control experiments were performed to compare the neutron transparencies of the two types of containers (Appendix C). The results for identical samples but different irradiation runs and containers agreed within the uncertainties and confirmed the absence of systematic differences between the two types of containers.

2.1.3. Irradiation

The samples were irradiated at the cyclotron laboratory at the Bern University Hospital (Inselspital). This 18 MeV compact medical cyclotron is operated daily for the production of ^{18}F, which is used in radiotracers for positron emission tomography (PET) (Auger et al., 2016; Braccini, 2016). ^{18}F is produced by bombarding liquid targets via the $^{18}O(p,n)^{18}F$ reaction. A rich multidisciplinary scientific program is ongoing along with the industrial production of radiotracers (Braccini, 2013, 2016; Braccini et al., 2011). The samples were placed in the so-called background position in the cyclotron bunker (i.e. not in front of the targets for ^{18}F production). The neutron energy spectrum was characterized by an spectrometer called DIAMON (direction-aware isotropic and active neutron MONitor with spectrometric capabilities; Pola et al., 2020) at this position. The signal processing and acquisition system included in DIAMON is conceived to continuously derive the 3D directional distribution of incoming neutrons in the energy range from thermal energy to 20 MeV. The neutron spectrum measured in the sample irradiation position is shown in Fig. 3 for an integrated beam current (IBC) of 0.15 μAh. The IBC is the total charge of the protons that hit the target during the irradiation run. As neutrons are generated by the proton-induced nuclear reaction $^{18}O(p,n)^{18}F$, the neutron fluence scales linearly with the proton beam current. The neutron fluence for each irradiation run was calculated from the IBC and is listed in Table 3. The relative neutron energy distribution was similar for all runs: approximately 40% of the neutrons were in the thermal energy state (0.025 eV), and 20% had >1 MeV. For comparison, a moderated neutron flux from an average crust material rock (Czubek, 1988) is shown in Fig. 3. Note the seven orders of magnitude difference between the artificial and natural neutron fluxes. Besides the difference in absolute amplitude, the energy distribution of the cyclotron neutrons peaks in the high energies (≥1 MeV), whereas natural neutrons (i.e. from average crust) show a flatter spectrum in this range. For an identical total ^{37}Ar production, a larger fraction would arise from fast neutrons activation

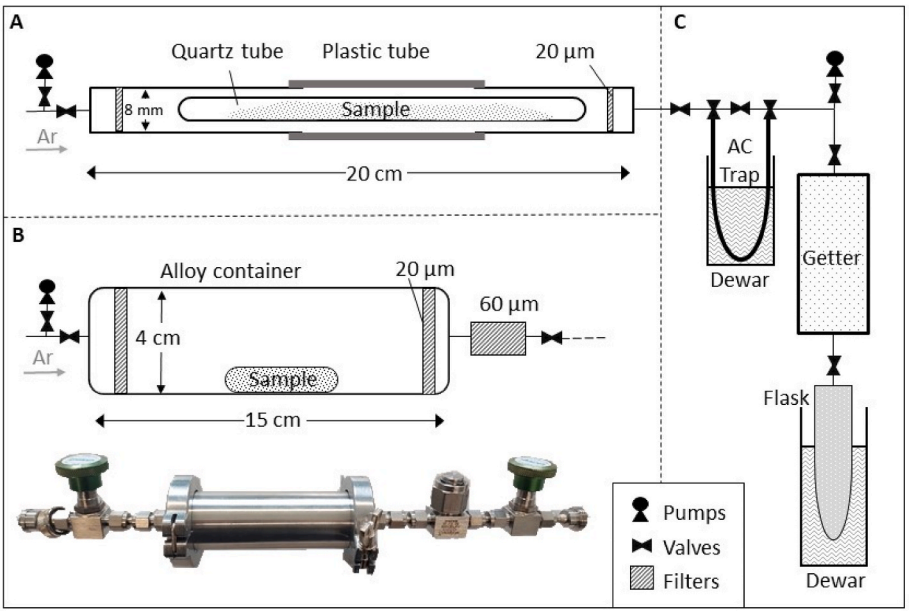

Fig. 2. Irradiation containers and transfer lines used to retrieve the emanated activity. A) Quartz tube in the cracker system; B) Alloy Vessel; C) Transfer line. Ultimately, the gas collected in the flask is used to fill low-level proportional counters.

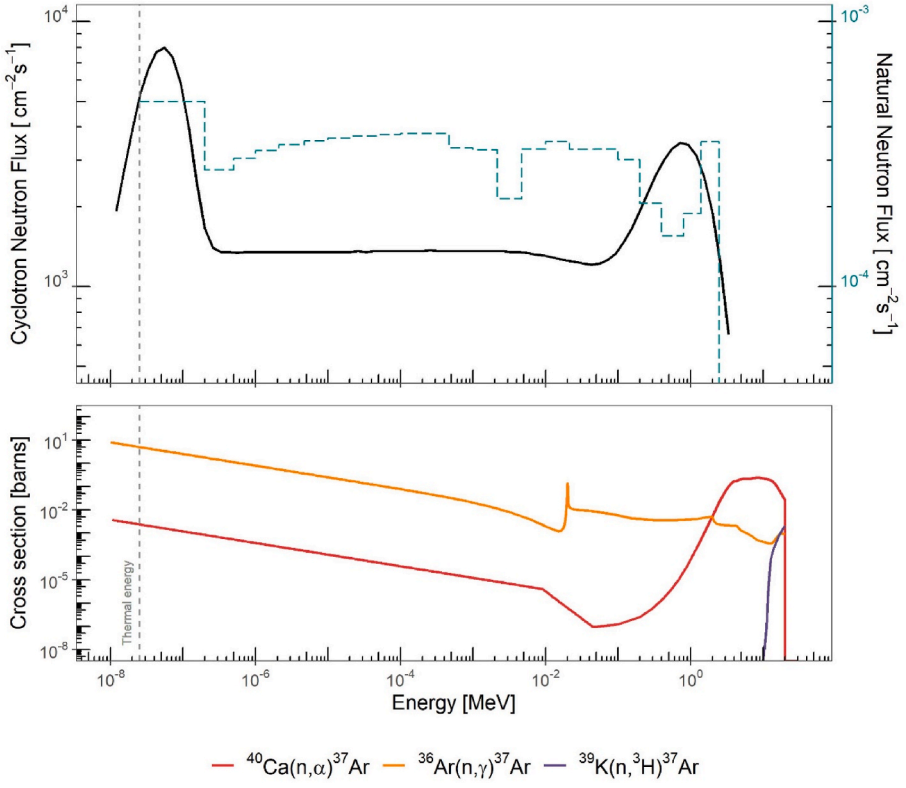

Fig. 3. (top) Measured neutron spectrum at the sample location in the cyclotron (black line) for an integrated beam current of 0.15 µAh, and moderated neutron spectrum from an average crust material rock (Czubek, 1988) (blue dashed line); (bottom) Reaction cross sections for the different ^{37}Ar production channels. (For interpretation of the references to color in this figure legend, the reader is referred to the Web version of this article.)

processes in the cyclotron; therefore, resulting in longer recoil ranges.

The ^{37}Ar production rate P_{37}, is the product of the concentration of target atoms N_{tg}, energy-dependent reaction cross section σ(E), and neutron flux Φ̇(E) (Eq.). The symbols used and units are listed in Table D-1 in Appendix D. The nuclear cross sections of the reaction channels for the ^{37}Ar production with incident neutrons from the database BROND-3.1 are presented in Fig. 3 (Blokhin et al., 2016). Integrating the cross-section and neutron flux resulted in the production rate per target atom (Table 2).

$$P_{37} = N_{tg} \int_0^{E_{max}} \sigma(E) \cdot \dot{\Phi}(E)\, dE \quad (1)$$

Table 2
^{37}Ar production channels. The production rate (per atom of target) resulting from the folding of the cyclotron neutron flux and the reaction cross section (Fig. 3) is normalized for IBC = 1 μAh. The contribution from each neutron energy range to the total production rate is also detailed.

Parent	Isotopic abundance	Reaction	Production rate[^{37}Ar s^{-1} N$_{tg}$ $^{-1}$]	Contributing neutron energy ranges [%]		
				Thermal (≤0.025 eV)	Epithermal (0.025 eV–1 MeV)	Fast (≥1 MeV)
^{40}Ca	0.9694	^{40}Ca(n,α)^{37}Ar	1.65×10^{-22}	1.2	37.6	61.2
^{36}Ar	0.0033	^{36}Ar(n,γ)^{37}Ar	1.06×10^{-19}	42.7	57.3	<0.1
^{39}K	0.9396	^{39}K(n,^{3}H)^{37}Ar	2.88×10^{-29}	0	0	100

Table 3
Neutron fluence (n_f), activity produced P_{37}, gross and net activities (A_{gross}, A_{net}), extrapolated background BG$_{ext}$, resulting emanation ε_T (Eq. (1)), and minimum detection activity (MDA) for all samples. The uncertainties on ε_T are absolute uncertainties. The activities are reported in mBq and corrected for decay between the end of the irradiation and the measurement. The P54-samples originate from Pleistocene glaciofluvial sediments.

Sample	n_f [cm^{-2}] × 10^{11}	P_{37}[Bq]			A_{gross}[mBq]			BG$_{ext}$[mBq]			A_{net}[mBq]			ε_T[%]			MDA [mBq]
Quartz tubes																	
$CaCO_3$ | 2.7 g	6.9	4.2	±	0.3	1.0	±	1.2	0.2	±	0.9	0.8	±	1.2	0.02	±	0.03	0.3
$CaCO_3$ | 5 g	6.9	7.7	±	0.5	2.3	±	0.8	0.2	±	0.9	2.0	±	0.8	0.03	±	0.01	0.2
$CaCO_3$| 8 g	6.9	12.3	±	0.9	4.3	±	1.0	0.2	±	0.9	4.0	±	1.0	0.03	±	0.01	0.1
$CaCO_3$| 5 g | 200 °C	6.9	7.9	±	0.6	5.2	±	1.7	0.2	±	0.9	4.9	±	1.7	0.06	±	0.03	0.3
$CaCO_3$| 5 g | 500 °C	6.9	7.6	±	0.5	106	±	3	0.2	±	0.9	105	±	3	1.4	±	0.1	0.2
$CaCO_3$| 5 g | 800 °C	6.9	7.8	±	0.6	776	±	4	0.2	±	0.9	776	±	4	9.9	±	0.7	0.2
P54-2	6.9	1.5	±	0.1	37	±	2	0.2	±	0.9	36	±	2	2.4	±	0.3	0.2
Alloy vessels																	
P54-1	13.1	20	±	1	1230	±	18	36	±	20	1195	±	38	6.0	±	0.6	1.3
P54-2	3.9	1.5	±	0.1	61	±	10	11	±	6	51	±	16	3.3	±	1.3	1.4
P54-3	3.9	2.0	±	0.2	44	±	9	11	±	6	33	±	15	1.7	±	0.9	1.3
P54-4	13.1	42	±	3	550	±	17	36	±	20	514	±	37	1.2	±	0.2	1.2
P54-5	3.9	2.2	±	0.2	50	±	8	11	±	6	40	±	14	1.8	±	0.8	1.3
P54-8	13.1	66	±	4	966	±	24	36	±	20	930	±	44	1.4	±	0.1	1.5
P54–B|> 2 mm	19.6	13.1	±	0.8	104	±	7	53	±	29	51	±	37	0.4	±	0.3	2.0
P54–B|2 mm–600 μm	3.9	3.8	±	0.3	27	±	5	11	±	6	27	±	11	0.7	±	0.4	1.7
P54–B|600 μm–212 μm	4.2	2.9	±	0.3	22	±	2	12	±	6	11	±	9	0.4	±	0.3	0.3
P54–B|212 μm–63 μm	19.6	12	±	1	127	±	9	53	±	29	127	±	38	1.0	±	0.4	1.3
P54–B|< 63 μm	4.2	2.9	±	0.3	27	±	3	12	±	6	16	±	9	0.5	±	0.4	0.9
Gneiss	4.2	0.32	±	0.04	33	±	3	12	±	6	22	±	9	6.8	±	3.8	0.3
Siliceous limestone	4.2	20	±	2	15	±	2	12	±	6	3	±	8	0.02	±	0.04	0.5
Yellow limestone | Dry	1.2	8.8	±	1.5	31	±	2	3	±	2	28	±	4	0.3	±	0.1	0.4
Yellow limestone | Wet	1.2	9.1	±	1.2	78	±	3	3	±	2	75	±	4	0.8	±	0.2	0.4

2.1.4. Activity retrieving and measurement

After irradiation, the samples were stored for >1 day, allowing the high activity short-living radioisotopes to decay. The activity emanated from the calcite powder in the quartz tubes was extracted using a cracker system consisting of two stainless-steel tubes joined with a flexible plastic tube (Fig. 2A). After evacuating the cracker system, the glass was broken by bending the plastic tube. The cracker volume was then flooded with pure argon (~1 bar) and left for 30 min, allowing for the entire gas phase to equilibrate, thereby highly minimizing the risk that a volume of gas emanated stays trapped in the quartz tube (i.e. a "dead gas" pocket). In the final step, the carrier argon and the sample were passed over a getter (Omni1000, NuPure) to remove the remaining reactive gases and cryogenically transferred to an activated charcoal-filled sample flask (Fig. 2C). This gas flushing and capturing procedure was repeated five times, resulting in a total argon volume in the flask of 1.4–2 L.

The procedure to recover the emanated activity in the alloy vessels was similar: the evacuated vessel was flooded with pure argon (at ~1 bar) and left for gas equilibration for 10–15 min. The gas was then transferred over the getter and into the flask at liquid N_2 temperature. The entire flood-retrieval procedure was repeated four times for each sample, resulting in an argon volume transfer of 1.5 L.

This transfer procedure was slightly adapted for the dry and wet limestone samples that were irradiated in a helium matrix. For these samples, an additional activated charcoal (AC) trap was placed on the transfer line between the vessel and capture flask (Fig. 2C). In this manner, argon, which was trapped at liquid N_2 temperatures, was separated from helium, which was not retained at this temperature and could be pumped out of the system.

Selected powder samples from the sediment powders and the two pebbles were stored in evacuated alloy vessels for 1–3 additional months before repeating the entire transfer procedure. The purpose of this procedure was to assess the efficiency of the initial transfer and investigate long-term emanation (Section 3.2).

For all samples, the gas was filled in proportional counters in the final step and measured by low-level counting (LLC) in the Deep Lab of the University of Bern (Riedmann and Purtschert, 2011). The decay corrected gross activities (A_{gross}) are reported in Table 3. Subtracting the background activity, which is described in the following section, results in the net activities (A_{net}). The total emanation ε_T is then calculated as following:

$$\varepsilon_T = \frac{A_{net}}{P_{37}} \tag{2}$$

2.2. Blanks and background activities

The pure carrier tank argon used to transfer the activity emanated to the counting system is subjected to ^{37}Ar production from cosmic ray neutron interactions. The resulting equilibrium activity concen tration at sea level is 1.06 (±0.15) mBq·kg$_{Ar}^{-1}$ (Saldanha et al., 2019). At 20 °C [ρ_{Ar} = 1.641 (±0.003) kg·m^{-3}], this corresponds to 1.3 (±0.1) × 10^{-6} mBq·cm$^{-3}_{STP,\ Ar}$. This is three orders of magnitude lower than the average tropospheric ^{37}Ar activity concentration of 10^{-3} mBq·cm$^{-3}_{STP,Ar}$

(Purtschert, 2017), for which the production by high-energy neutrons in the high atmosphere and stratosphere layers represents the most significant source. The minimum detectable activity (MDA) is the activity allowing the detection of a peak with 95% confidence level. For each sample, the MDA is calculated as described in Riedmann and Purtschert (2011) (Table 3). In general, for typical measurement conditions (50 cm^3 counter filled at 10 bars, 0.47 counting yield), it is about 8×10^{-4} mBq·cm^{-3}_{Ar}. Thus, the specific activity concentration of the tank argon can be neglected.

Several background measurements were performed in both types of irradiation containers without samples. Background counts could originate from filters, seals, air contamination, and cross-sample contamination after cleaning and reusing the alloy containers. The activities measured in these blanks as a function of the neutron fluence from their irradiation runs are presented in Fig. 4. The quartz tube blank irradiation resulted in an activity of 0.2 (±0.9) mBq (Table 3), which is in the order of the MDA for this sample. A first blank measurement of the empty alloy vessels resulted in an activity of 0.84 (±0.07) mBq, for a neutron fluence of 3.9×10^{-11} n·cm^{-2} (IBC = 1183 μAh), which is also in the MDA range. However, subsequent measurements in all vessels resulted in blank activities of up to 25 (±2) mBq, with some correlation with neutron fluence (Fig. 4). Contamination of the vessel filters or the different elements along the transfer line (getter and tubes) was excluded by subsequent laboratory tests. The linear dependency of the background activity on the neutron fluence points to the production by interfering reactions. The most critical one is ^{37}Ar production on ^{36}Ar contained in the remaining traces of air in the sample, or from the outgassing of filters and rubber sealings. In the neutron energy range <2 MeV, the ^{36}Ar(n,γ)^{37}Ar reaction has a larger cross-section than that of ^{40}Ca (Fig. 3). To explain the observed scatter of background values, air volumes of 5–15 μL_{STP} (^{36}Ar/Ar = 0.33%) are sufficient (shaded area in Fig. 4). This corresponds to a residual pressure of ~0.05 mb in the 180 cm^3_{STP} containers, which is slightly higher than the vacuum applied prior to irradiation (<0.01 mb). The reason for the marginally elevated background values could not be conclusively identified. Based on the neutron fluence n_f for each measurement in the alloy vessels, background values were estimated as BG_{ext} [mBq] = $2.7 \times 10^{-11} \cdot n_f$ (solid line in Fig. 4 and values in Table 3).

In the cyclotron, as well as underground, ^{37}Ar is primarily produced by the $^{40}Ca(n,\alpha)^{37}Ar$ reaction channel owing to the predominance of calcium atoms. Our emanations refer only to the calculated activity estimated for this production channel. Interfering reactions, defined as reactions occurring on targets other than ^{40}Ca, would thus lead to an emanation overestimation. The possible reaction on potassium, ^{39}K(n,^{3}H)^{37}Ar, is insignificant owing to the very small reaction cross-section for neutron energies <9 MeV (Fabryka-Martin, 1988).

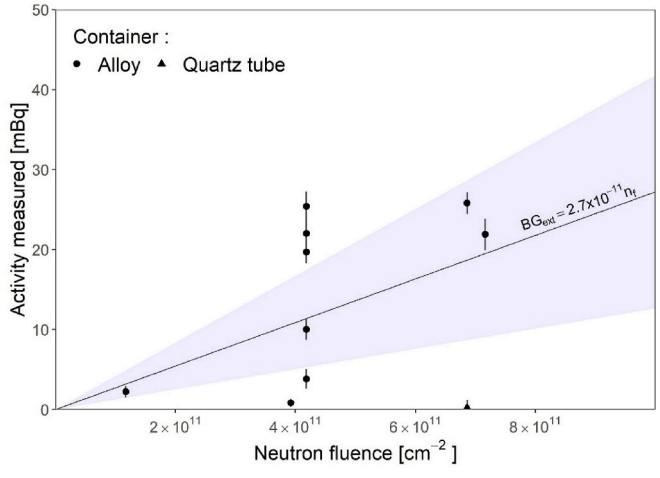

Fig. 4. Background measurements: ^{37}Ar activity produced as a function of the neutron fluence (calculated from the IBC) during the irradiation of the empty containers. The solid line is the linear least squares regression with the neutron fluence. Air volumes of 5–15 μL would result in background values indicated by the shaded area [from the reaction ^{36}Ar(n,γ)^{37}Ar]. This also corresponds to the 95% confidence interval of the linear fitting. The average MDA for the blank irradiation conditions is 0.44 mBq (not visible).

3. Results

3.1. Emanation fractions

The emanation fractions at room temperature for all the experiments are summarized in Fig. 5. The lowest emanation fractions in the powdered samples were observed for calcite, with a median value of 0.03 (±0.01)%. In addition, the $CaCO_3$ powder samples were used to confirm the constant production rate dependency on the mass of calcite at room temperature (Appendix E). For the sediment powder, an emanation of 1.8 (±0.6)% was obtained, whereas particle sizes ranging from 63 μm to 2 mm resulted in 0.5 (±0.3)% emanation (Table 3). The errors represent the standard deviations of the emanation values for each sample type and are absolute uncertainties. For the pebbles, the emanation was calculated from the activity measured directly after irradiation (A_{net}), as well as from the total activity after a storage time of approximately one month (described in Section 3.2, Table 4). These activities resulted in emanations of 7 (±4)% and 10 (±5)%, respectively, for the gneiss and 0.02 (±0.04)% and 0.07 (±0.06)%, respectively, for the siliceous limestone. Finally, the emanation fractions for the dry and wet limestone were 0.3 (±0.1)% and 0.8 (±0.2)%, respectively.

3.2. Sample storage

The results presented in the previous section correspond to the activity released shortly after irradiation. Selected samples were stored in an evacuated irradiation container for 1–3 months before repeating the transfer procedure. The residual activity A_S was then corrected for radioactive decay and compared to the net activity measured initially (A_{net}, Table 4). In the sediment powder samples, this residual fraction was between 0.3% and 12.6% of the previous net activities. In contrast, the residual fraction was 41% for the gneiss and 350% for the siliceous limestone. The sum of instantaneous and delayed released activities (last column in Table 4) is then compared with the calculated activity

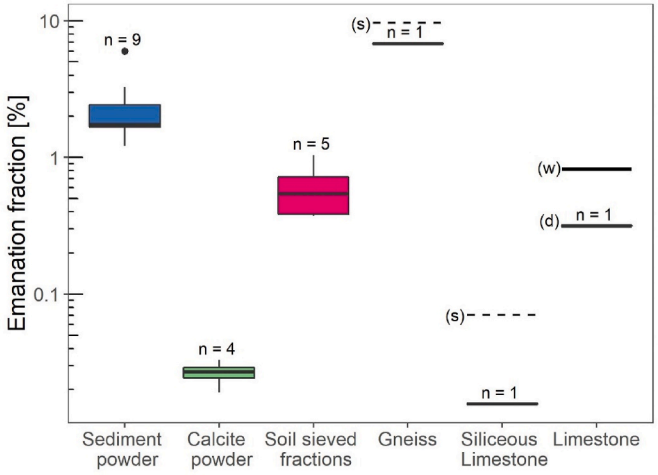

Fig. 5. Emanation fractions at room temperature. Lines (with ranges) refer to measurements shortly after irradiation. The dashed line for the gneiss and the siliceous limestone corresponds to the total emanation after one month of storage (s) (Table 4; Sections 3.2 and 4.5). Limestone values were measured for dry (d) and wet (w) samples. n refers to the number of measurements and the dot for the sediment powder is an outlier.

Table 4
Activity measured shortly after the irradiation (A_{net}) and activities A_S that emanated during an additional storage time of 1–3 months (decay corrected). The total activity is the sum of A_{net} and A_S.

	A_{net} [mBq]	Activities after storage A_S [mBq]			Residual fraction [%]			Total activity [mBq]
		1 month	2 months	3 months	1 month	2 months	3 months	
P54-1	1195	7.8 ± 2.0		3.3 ± 1.9	0.65 ± 0.17		0.27 ± 0.16	1206 ± 40
P54-2	51		3.1 ± 3.0			6.05 ± 6.27		53.7 ± 17.1
P54-3	33		4.2 ± 2.3			12.59 ± 8.94		37.5 ± 15.4
P54-4	514	4.6 ± 1.7			0.90 ± 0.34			519 ± 33
Gneiss	22	8.9 ± 2.4			41.4 ± 20.6			30.5 ± 8.2
Siliceous limestone	3.2	11.2 ± 2.7			350 ± 255			14.4 ± 9.4

produced P_{37} (Table 3), resulting in total emanation fractions of 9.5% for the gneiss resp. 0.07% for the siliceous limestone (dotted lines in Fig. 5). This delayed release is discussed in the context of diffusion emanation in Section 4.5.

4. Discussion

4.1. Conceptualization of the emanation process

The emanation process from the macroscopic samples can be described using a two-step process. First, the nuclide was transferred from the solid mineral phase into a pore space by instantaneous recoil. This process is described by recoil theories [(Onstott et al., 1995); Section 4.2] and is called the emanation power in the context of ^{222}Rn emanation (Semkow, 1990). The volume and geometry of the pore space in which the nuclide, in our case ^{37}Ar, is released, depend on the scale of the system considered. This can range from the internal structure of a grain (Fig. 6A) or a solid piece of rock (Fig. 6B) to a coarser porosity in the case of an aggregate of smaller sub-clasts (Fig. 6C). Herein, it is assumed that the production is homogeneous in all sub-compartments.

In the second step, the released nuclides migrate by time-dependent diffusion from the internal pore space to an outer macroscopic pore volume, where it is eventually sampled and measured (Section 4.5). The transport process from the site of production (i.e. the rock) to the volume available for advective transport is especially important during groundwater extraction in aquifers and gas extraction in soils. These methods are carried out in boreholes and drain the most conductive parts of the system, and therefore inherently resulting in flow averaged concentrations (Musy et al., 2021). This is especially the case for ^{37}Ar, where large sample volumes are required for analysis (Loosli and Purtschert, 2005). Assessing the emanation at the aquifer scale (Fig. 6D) is then essential to constrain the importance of underground production in the activities measured.

In ^{222}Rn literature, diffusion through the pores of macroscopic samples is called exhalation (Sakoda and Ishimori, 2017). This is not to be confused with solid-phase diffusion in the crystal lattice that occurs simultaneously with recoil emanation (Flügge and Zimens, 1939; Maraziotis, 1996). This slow process can be neglected at ambient temperature for ^{37}Ar because of its relatively short half-life but becomes significant at higher temperatures (Section 4.4).

In nature, both the recoil and diffusion processes occur simultaneously in a production-decay-loss steady-state equilibrium. In contrast, in irradiation experiments, highly transient conditions prevail because production occurs over a much shorter timescale than the half-life of ^{37}Ar. We define the total emanation fraction ε_T, which is given by the product of the recoil emanation ε_R and macroscopic diffusion emanation (or exhalation) ε_D (Eq. (3)). Note that these two processes occur successively and are therefore described as a product in Eq. (3) in contrast to simultaneous processes, which would be parameterized by a sum. In the following section, we interpret our data using this simple concept. For a spherical grain with radius r_0 and recoil range R, the recoil emanation ε_R is described by Eq. (4) (Flügge and Zimens, 1939). When $2r_0 \gg R$, the second term can be neglected. Similarly, the steady-state diffusive emanation fraction ε_D can be defined from the particle size and effective diffusion coefficient D (Eq. (5)) for spherical conglomerates with radii larger than the diffusion length ($r_0 > L$). For short times t

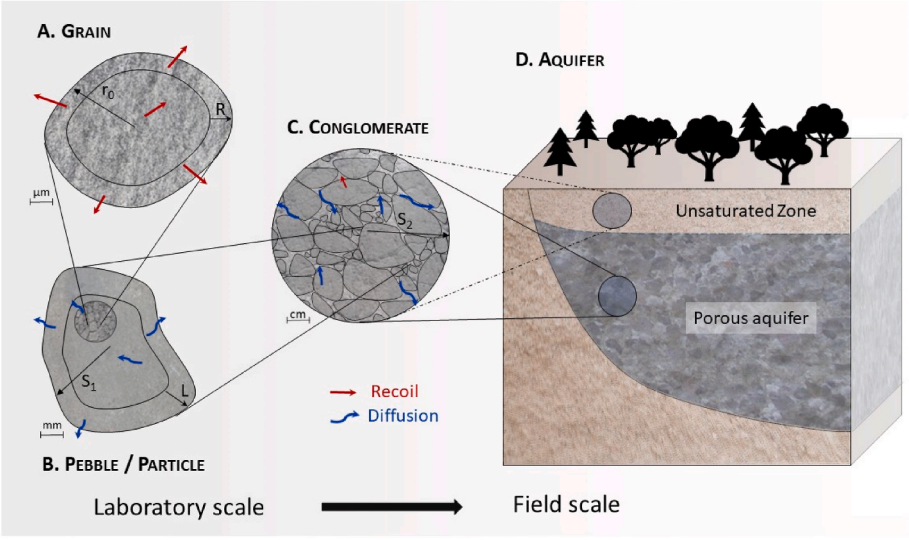

Fig. 6. Conceptualization of the emanation process on different spatial scales. A) Recoil emanation from a spherical grain with a radius r_0 and recoil range R followed by B) diffusive migration from macroscopic samples (particle) of size S1 and diffusion length L or C) from conglomerates of dimension S2 in D) natural systems. Our experiments provide information about the scales A) and B).

$\ll T = \lambda^{-1}$, the diffusion length L can be replaced by the depletion layer x_d [Eq. (6), Jourdan et al. (2007)].

$$\varepsilon_T = \varepsilon_R \cdot \varepsilon_D with\ \varepsilon_T \leq \varepsilon_R \tag{3}$$

$$\varepsilon_R = \frac{3}{4}\frac{R}{r_0} - \frac{1}{16}\left(\frac{R}{r_0}\right)^3 for\ 2r_0 \leq R \tag{4}$$

$$\varepsilon_D = 3 \cdot \frac{L}{r_0} with\ L = \sqrt{\frac{D}{\lambda}} \tag{5}$$

$$x_d = \sqrt{D \cdot t} \tag{6}$$

The recoil range R of particle B, produced in a nuclear reaction of type $A(a,b)B$, depends on the momentum of the incident particle a, the masses of the reaction partners involved *(A, b,* and *B)*, the reaction energy, and the density of the surrounding media. The recoil range of the reaction $^{40}Ca(n,\alpha)^{37}Ar$ in a medium with a density $\rho = 2.6$ g cm^{-3} has been estimated to be in the range of 0.1–0.3 μm (Onstott et al., 1995).

4.2. Recoil-dominated emanation

In irradiated pulverized samples, recoil emanation is likely the dominant process to consider, while diffusion is of minor importance. For a given recoil range, it is expected that the finer the powder, the larger the emanation fraction. The higher emanation observed in the sediment powder than in the calcite powder is attributed to the grain size difference. The average grain size ($= 2r_0$) of the calcite powder was 17 μm and only 1.9 μm in the sediment powder samples (Table 1). Using Eq. (4) with $R = 0.2$ μm, the theoretical recoil emanation was 18% for the sediment powder and 1.7% for the calcite powder. However, these values must be regarded as upper estimates because the process of implantation in the adjacent grain is not considered. If a recoiled atom has sufficient energy to cross the pore space, it can eventually end its course in the opposite grain, thereby reducing the fraction of recoil emanation (Fleischer, 1983). Therefore, assessing the effect or an average longer recoil range, associated for instance with a larger fraction of activity produced by high energy neutrons (as it is the case in the cyclotron, see Section 2.1.3) requires consideration of the pore geometry and saturation conditions.

The expected smaller emanations with increasing grain size seem to contradict the relatively uniform emanation values observed in the sieved material over a grain size range of 63 μm – 2 mm (Table 3, Fig. 7). The different sieved fractions can be seen as diversely sized aggregates of the same material (Fig. 6A and B). The recoil emanation is similar for all particle sizes of the same material because it depends on the grain packing, that is, the inner particle porosity (Peng et al., 2012). Assuming an effective pore diffusion coefficient of $D_{eff} = 10^{-11}$ m^2 s^{-1} (see below), the depletion layer over one week is $x_d \cong 2$ mm (Eq. (6)), which is sufficient for the total diffusion of the activity out of the particles, even for the largest ones.

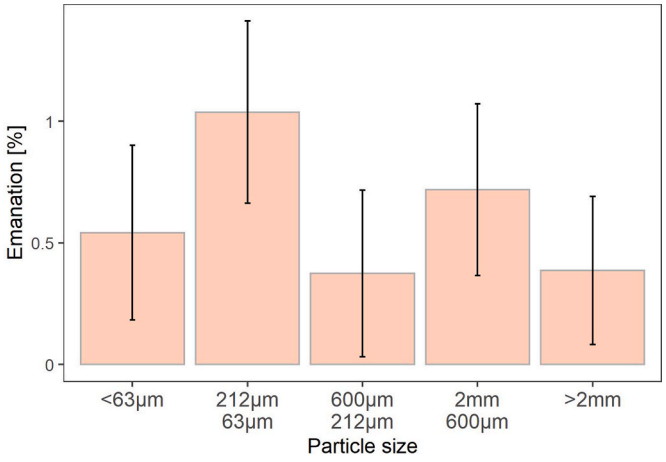

Fig. 7. Dependency of the emanation on the particle size in samples of differently sieved fractions.

After the first ^{37}Ar extraction procedure, the powdered sediment samples were stored for a second time for several weeks to investigate delayed release owing to diffusion out of the samples. Only a very minor fraction of total production resided in the samples after 1–3 months (0.2–12.5%, Table 4), which indicates that the yield of the extraction procedure (Section 2.1.4) was high, but also that emanation after irradiation occurred predominantly by recoil in the powdered samples. A different situation can be expected for the macroscopic samples (Section 4.5).

4.3. ^{37}Ar emanation in soil

The measured emanation fractions of the powdered sediment showed a clear trend with the depth from which the samples were collected (Fig. 8A, Table 3). Soil is defined as unconsolidated organic or mineral material on the immediate surface of the Earth. In our case, this likely represents the top few decimeters of the sediment core. The chemical and structural soil constitution is strongly influenced by weathering processes, which decrease with increasing soil depth (Burke et al., 2009; Suther et al., 2021). The degree of soil-weathering can be parameterized by chemical weathering indices (CWIs), which are commonly characterized by measuring the ratios between "immobile" and "mobile" oxides (Delvaux et al., 1989; Price and Velbel, 2003). Fig. 8B shows that the emanation fractions increase with Vogt's residual index V (Liu et al., 2014), which characterizes the degree of weathering and hence the fraction of fine clay minerals in the shallow soil horizons. The positive correlation can be understood by the high cation exchange capacity (CEC) of clay minerals (CUCE, 2007; Radulov et al., 2011). Thereby, negatively charged sites on clay minerals and organic matter surfaces adsorb cations, including Ca^{2+}, and prevent their downwards leaching. This results in the agglomeration of Ca^{2+} ions at the external surface of the grains, thus enhancing ^{37}Ar production by the $^{40}Ca(n,a)^{37}Ar$ reaction at sites from which ^{37}Ar easily escapes.

4.4. Diffusion in crystal lattices

In a mineral grain, the radionuclides that did not escape by recoil may still diffuse in the crystal lattice. This so-called "solid diffusion" contributes to the total activity emanated in the pore space and is thus available for pore diffusion (i.e. exhalation). To constrain the solid diffusion coefficients, a heating experiment was performed using $CaCO_3$ powder samples ($m = 5.0 \pm 0.1$ g). After irradiation, the samples were placed in a furnace for 8 h at either 200 °C, 500 °C, or 800 °C before being transferred. The total emanation fraction ε_T was measured for each temperature (Fig. 9A). As solid diffusion and recoil emanation occur concurrently, ε_T is the sum of the constant recoil emanation ε_R and temperature-dependent diffusion emanation $\varepsilon_{Ds}(T)$ (Eq. (7)).

$$\varepsilon_T(T) = (\varepsilon_R + \varepsilon_{D_s}(T)) \tag{7}$$

For a heating time much shorter than the half-life ($t \ll T_{1/2}$), Eq. (8) applies to the relationship between diffusive emanation $\varepsilon_{Ds}(T)$ and the diffusion parameter D_S (Flügge and Zimens, 1939). $D_S(T)$ was then calculated for each temperature (Fig. 9B) using Eq. (9) and fitted using the Arrhenius equation (Eq. (10)). The activation energy E_a and frequency factor D_0 can be derived from the slope and y-intercept of the regression line, respectively, and ε_R is a free-fitting parameter for the regression. The resulting $\varepsilon_{Ds}(T)$ calculated from $D_S(T)$ in Eq. (8) are shown in Fig. 9A.

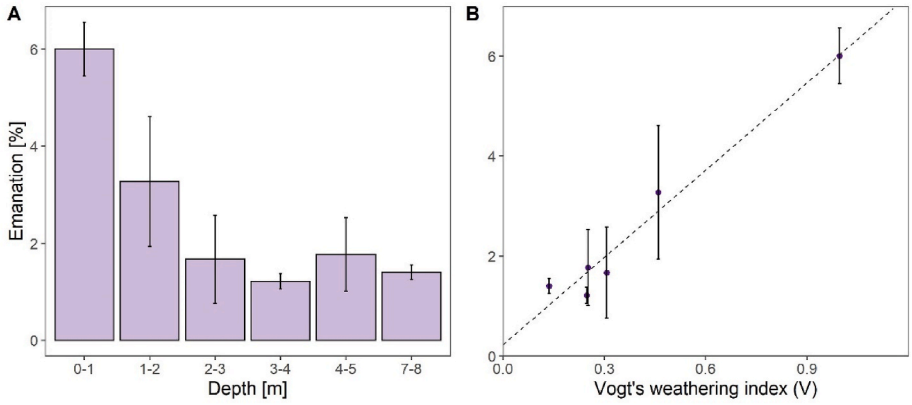

Fig. 8. Emanation dependency on A) depth bellow surface in the sediment powder samples; B) Vogt soil weathering index determined from the measured soil composition in Table A-1.

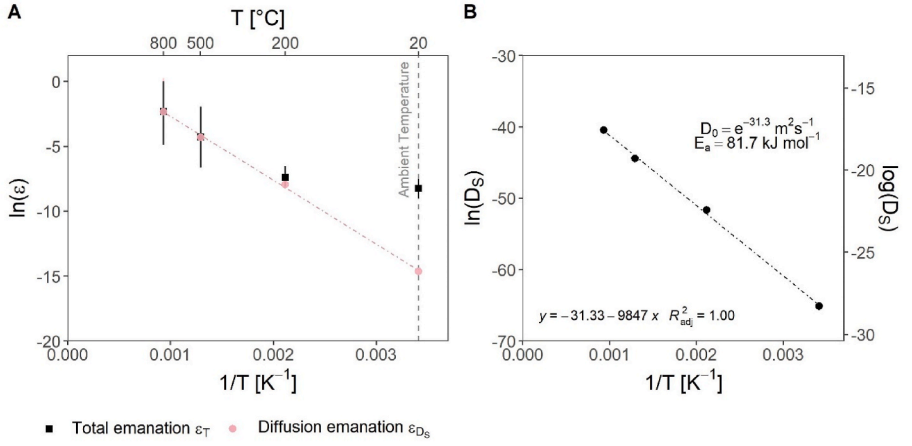

Fig. 9. A) Relationship between the emanations ε_T (black squares) and ε_{Ds} (pink dots) of the heated $CaCO_3$ measurements and the temperature (T) ; the pink line is the linear regression of ε_{Ds} with $\varepsilon_R = 0.026\%$. B) Arrhenius plot (Eq. (10)); the linear relationship between the solid diffusion coefficient D_S calculated with Eqs. (9) and $1/T$. (For interpretation of the references to color in this figure legend, the reader is referred to the Web version of this article.)

$$\varepsilon_{Ds}(T) = (\varepsilon_T(T) - \varepsilon_R) = \frac{3}{r_0}\cdot\sqrt{D_s(T)\cdot t} = C\cdot\sqrt{D_s(T)} \quad \text{with } C = \frac{3\cdot\sqrt{t}}{r_0} \tag{8}$$

$$D_s(T) = (\varepsilon_T(T) - \varepsilon_R)^2\cdot C^{-2} \tag{9}$$

$$D_s(T) = D_0\cdot e^{-\frac{E_a}{R}\frac{1}{T}} \tag{10}$$

The linearity of the data ($R^2 = 1$) indicates a single-domain diffusion of Ar in calcite over the tested temperature range (Harrison and Lovera, 2014). The $\varepsilon_R = 0.026\%$ resulting from the linear fitting agreed with the median value for calcite powders at room temperature (Fig. 5). The activation energy E_a = 81.7 kJ mol^{-1} derived from the slope of the Arrhenius equation is comparable to the values concluded for plagioclase [85 kJ mol^{-1} (Schwarz, 2001);] or quartz [51 kJ mol^{-1} (Watson and Cherniak, 2003);]. The diffusion coefficient at room temperature was $D_s = 5.3 \times 10^{-29}$ m^2 s^{-1}, which is consistent with previous estimates in the order of 10^{-26} – 10^{-28} m^2 s^{-1} (Riedmann and Purtschert, 2011; Watson and Cherniak, 2003). These values resulted in a diffusion length of <1 nm, therefore not allowing any significant solid-diffusion emanation in a grain >1 μm before ^{37}Ar decays.

4.5. Emanation from macroscopic samples

In contrast to the powder samples, the pebbles showed much larger remaining activities after a one-month storage (Table 4), indicating diffusive transport at a larger scale. After the atoms are released by recoil, this macroscopic diffusion may take place along crystal imperfections, grain boundaries, or in an inner network of nanopores (Rama and Moore, 1984) like for instance, alpha-recoil tracks (so-called "radiation damages") (Guenthner et al., 2013; Morawska and Phillips, 1992). Consequently, the resulting effective diffusion coefficient D_{eff} in the pore space is scale-dependent (Lehmann and Purtschert, 1997). For a given scale and radioactive tracer, a slower diffusion (linked with a smaller D_{eff}) leads to a delayed emanation process, allowing more time for the radioactive decay and therefore an overall lower emanation fraction.

The delayed release observed during sample storage was interpreted in the framework of a transient diffusion transport model for spherical grains with radius r_0. The concentration C_P of ^{37}Ar within the micropore space after recoil is given by Eq. (11), with the initial condition $C_P(r, 0) = C_0 = P_{37}\cdot\varepsilon_R$ being the activity concentration recoiled in the pore space instantaneously after the irradiation. The activity at the outer pebble boundary was assumed to be constant $C_P(r = r_0, t) = 0$. The differential equation was solved numerically using the R-Package ReacTran (Soetaert and Meysman, 2012). The flux $J(t)$ escaping the pebble with surface area S, as described by Fick's first law (Eq. (12)), decreased exponentially with time owing to mass conservation and radioactive decay.

$$\frac{\partial C_p(r,t)}{dt} = D_{eff}\frac{\partial^2 C_p(r,t)}{\partial r^2} - \lambda C_p(r,t) \tag{11}$$

$$J(t) = S \cdot D \cdot \left.\frac{\partial C_p}{\partial r}\right|_{r=r_0} \tag{12}$$

$$\frac{\partial C_v(t)}{dt} = J(t) - \lambda C_v(t) \tag{13}$$

The build-up of activity C_V in the storage container (Eq. (13)) was then fitted to the measured data with free parameters ε_R and D. The transfer procedure resets the activity in the container; therefore, the total emanated activity $C_{V,tot}$ is the sum of the activities measured before and after storage (at t_1 and t_2). The measured activities from Table 5 were not decay-corrected because radioactive decay is included in the model.

In the fitting procedure, ε_R controls the initial activity in the pore space C_0; thus, the magnitude of the signal is released, whereas D_{eff} controls the kinetics of the gas, that is, the time of maximal activity. Both ε_R and D_{eff} were optimized for the model to reproduce the activities measured within the uncertainties (95% confidence interval). The highest possible recoil emanation (ε_R = 100%) is associated with the lower limit of the diffusion coefficient D_{min}. Equivalently, the upper limit D_{max} is projected with the minimum ε_R, which is restricted by the lowest possible C_0 that allows the simulation of the measured activities.

The resulting ranges of D_{eff} were $2.2 \times 10^{-12} - 2.5 \times 10^{-11}$ m^2 s^{-1} and $1 \times 10^{-16} - 9 \times 10^{-12}$ m^2 s^{-1} for the gneiss and siliceous limestone, respectively. The ε_R for the gneiss was 45–100% and for the limestone 0.4–100% (colored ribbons in Fig. 10). These values are in good agreement with the order of magnitude of radon diffusion coefficients in sandstones and granites reported by Liu et al. (2014) and Lehmann and Purtschert (1997), and many orders of magnitude larger than D_s concluded for $CaCO_3$ (Table 5).

In the simulation, a spatially and temporally constant diffusion coefficient D_{eff} was assumed. However, diffusion occurring in larger pores (with larger D_{eff}) in the first place, might be followed by diffusion in smaller pores in a second step. Such scale-dependent diffusion might be the reason for the increasing trend observed in the data, in contrast to the simulation.

4.6. Water influence on emanation

The influence of the presence of water on the emanation values was assessed by comparing the values of dry and wet limestones. Special attention was paid to the fast transfer of the wet sample in a helium atmosphere to avoid contact with air. In addition, the time between this transfer and the irradiation was minimized to avoid the drying of the sample. The emanation values were 0.3 (±0.1)% and 0.8 (±0.2)% for the dry and wet limestone samples, respectively (Fig. 5). This enhancement is explained by the higher stopping power of water compared with air, resulting in shorter recoil ranges. Therefore, recoiled atoms are more likely to be trapped in the pore space before implantation in the adjacent grain. Adler and Perrier (2009) and Sun and Furbish (1995) demonstrated that radon emanations reach maximal values from moisture contents of 20–40%. Radon emanation coefficients in saturated residues were reported to be 2–6 times higher than in dry residues

Table 5
Net activities $C_{V,m}$ measured before and after the storage of the pebble samples [group (iv)]. t_1 = 17 days is the time elapsed between the end of the irradiation and the first measurement; t_2 = 48 days is the time between the end of the irradiation and the second measurement. The total activity $C_{V,tot}(t_2) = C_{V,m}(t_1) + C_{V,m}(t_2)$.

	$C_{V,m}(t_1)$ [mBq]	$C_{V,m}(t_2)$ [mBq]	$C_{V,tot}(t_2)$ [mBq]
Gneiss	21.4 ± 2.7	3.6 ± 1.0	25.0 ± 7.4
Siliceous limestone	8.0 ± 2.1	3.9 ± 0.9	11.9 ± 4.2

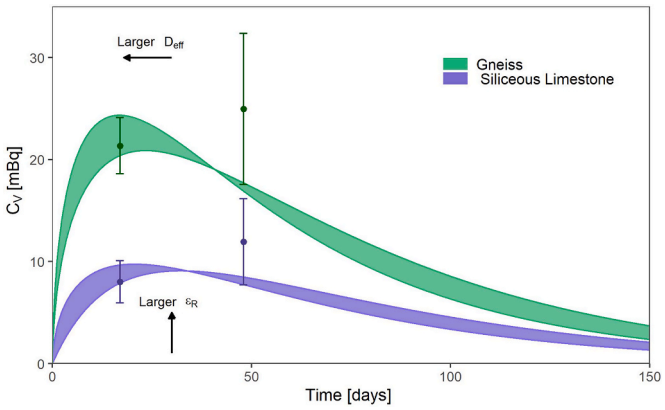

Fig. 10. Activity measured in the irradiation containers for the gneiss (green) and siliceous limestone pebbles (purple) (Table 5). The curves are calculated with the numerical solution of Eq. (13) for an inner porosity of φ = 1%, a radius r_0 = 1 cm and for produced activities P_{37} = 20.4 Bq in siliceous limestone and P_{37} = 0.317 Bq in gneiss. The areas represent the feasible range of D_{eff} and ε_R. (For interpretation of the references to color in this figure legend, the reader is referred to the Web version of this article.)

(Fleischer, 1983; IAEA, 2013; Sakoda and Ishimori, 2017; Semkow, 1990), which is in agreement with the value we observe.

Therefore, water has two counteracting effects, and the prevalence of one or the other depends on the saturation conditions and the scale considered. For example, in small particles in aquifers, where recoil dominates, water enhances the emanation. On a macroscopic scale, where diffusion in the pore space is important, water slows down the diffusion process. Diffusion coefficients in water are approximately four orders of magnitude smaller than those in air, leading to an overall reduced emanation in water filled pores. The observed apparent recoil emanation enhancement in the presence of water might therefore be partly masked by diffusive retardation.

5. Summary and conclusion

Using underground produced radioactive gas tracers for groundwater dating or nonproliferation purposes relies on knowledge of the production rate and the transfer process from the production site to the sampling point. The latter process is characterized by emanation, that can be described by a two-step mechanism, where the atoms produced are first recoiled into the pore space where diffusion occurs. As both processes are significant for the interpretation of field data, we addressed not only the recoil emanation fractions on the microscopic scale, but also the delay of ^{37}Ar escape owing to diffusive transport on macroscopic scales in our experiment.

Instantaneous ^{37}Ar recoil emanations $\leq$ 1% were observed in powdered dry sediments and $CaCO_3$ samples. This is at the lower edge, but consistent with previous estimates (Johnson et al., 2021; Krishnaswami and Seidemann, 1988; Loosli et al., 1989). In soils, a clear depth-related systematic is observed with increased emanation fractions owing to weathering processes close to the surface. This effect induces differences of almost one order of magnitude over a few meters and has implications for the interpretation of the natural soil gas ^{37}Ar background (Carrigan et al., 1996; Haas et al., 2010; Riedmann and Purtschert, 2011). The first proof of principle assessment of the effect of water on recoil emanation indicates an enhancement of the recoil emanation fraction of at least a factor three in wet limestone compared to dry rock.

Surprisingly, the recoil emanation fraction in rock pebbles was not necessarily smaller than that in the powdered samples. This is likely the result of nanopores and structural imperfections within the macroscopic mineral rock samples. At this scale, the release of ^{37}Ar to the outer sample boundary was controlled by diffusive transport. We estimated

diffusion coefficients in the range $10^{-12} > D > 10^{-16}$ m^2 s^{-1} and diffusion lengths of 2 mm $\geq L \geq$ 20 μm for gneiss and a siliceous limestone pebble. This implies that only a fraction of the rock volume contributes to its total emanation. This delayed diffusion emanation may explain why the significance of underground production (e.g., for ^{39}Ar) is relatively weakly correlated with the U and Th concentrations of the host rock but is linked to the aquifer type (Purtschert, 2012).

Diffusion emanation from the solid $CaCO_3$ mineral phase was investigated using a heating experiment. The resulting diffusion coefficient of the order of 10^{-29} m^2 s^{-1} at 20 °C confirms that solid-phase diffusion emanation can be neglected for ^{37}Ar (and ^{39}Ar) applications. In addition, our diffusion parameters and activation energies for argon in $CaCO_3$ are consistent with literature values. This indicates that the proposed experimental procedure provides a coherent framework for the assessment of the emanation fractions in natural samples. In our experiments, we used a neutron field produced in a routinely operated medical cyclotron for the first time. The relatively easy access to such facilities offers promising and innovative possibilities for addressing transdisciplinary research questions. Similar experiments could be realized in the future by using higher-energy neutrons, for example, for ^{39}Ar emanation experiments.

Declaration of competing interest

The authors declare the following financial interests/personal relationships which may be considered as potential competing interests: Stephanie Musy reports financial support was provided by Swiss National Science Foundation.

Acknowledgments

This work was partially supported by the Swiss National Science Foundation (Grants: 200020, 172550, CRSII5_180352). The authors are grateful to Kurt Grossenbacher and Remo Walther from the University of Bern for their precious technical support in the laboratory. We acknowledge contributions from LHEP engineering and technical staff and we are thankful to the SWAN Isotopen AG team for the collaboration. In addition, we thank the two anonymous reviewers and the associate editor for their constructive comments, which helped to improve this manuscript. Finally, we are grateful to Jean-Elie Fontaine for his help assessing the production rates.

A. Rock composition

Table A-1
Elemental composition for the natural sediment and rock samples (group ii-v).

Group	Sample	SiO_2	Al_2O_3	Fe_2O_3	MnO	MgO	CaO	Na_2O	K_2O	TiO_2	P_2O_5	LOI	Si	Al	Fe	Mn	Mg	Ca	Na	K	O	Th	U
		[wt.%]											[wt.%]									[ppm]	
(ii)	**P54–1**	62.0	8.7	3.2	0.1	1.2	8.1	1.0	1.6	0.4	0.1	13.0	29.0	4.6	2.3	0.1	0.7	5.8	0.7	1.3	41.7	6	1.8
	P54–2	65.2	5.4	2.2	0.1	0.9	12.6	0.8	1.1	0.2	0.1	11.5	30.5	2.9	1.5	0.1	0.5	9.0	0.6	0.9	42.4	5.3	1.6
	P54–3	61.9	4.4	1.5	0.1	0.6	16.1	0.8	1.0	0.2	0.1	13.4	28.9	2.3	1.0	0.1	0.4	11.5	0.6	0.8	40.8	5.8	1.8
	P54–4	61.8	3.7	1.5	0.1	0.6	17.0	0.6	0.8	0.1	0.1	14.1	28.9	2.0	1.0	0.0	0.4	12.1	0.5	0.7	40.6	4.1	1.1
	P54–5	54.4	4.4	1.8	0.1	1.1	18.8	0.7	0.8	0.2	0.1	16.5	25.4	2.3	1.2	0.0	0.7	13.4	0.5	0.6	37.8	3.1	1
	P54–8	44.3	3.2	2.2	0.2	1.0	26.5	0.5	0.6	0.1	0.1	22.2	20.7	1.7	1.5	0.1	0.6	18.9	0.4	0.5	34.1	3.4	1.1
(iii)	**P54–B**	63.5	4.9	1.8	0.1	0.7	14.4	0.8	1.1	0.2	0.1	12.5	29.7	2.6	1.3	0.1	0.4	10.3	0.6	0.9	41.6	3.8	1.2
(iv)	**Gneiss**	74.3	12.1	4.1	0.1	1.3	0.6	2.5	2.9	0.5	0.1	1.9	34.7	6.4	2.9	0.0	0.8	0.4	1.9	2.4	48.6	9.6	2.2
	Siliceous limestone	30.5	0.2	0.3	0.0	0.5	37.0	0.1	0.0	0.0	0.0	29.1	14.2	0.1	0.2	0.0	0.3	26.4	0.0	0.0	27.2	0.3	0.3
(v)	**Yellow limestone**	9.5	0.9	1.5	0.1	0.3	47.1	0.1	0.3	0.1	0.1	30.6	4.4	0.5	1.0	0.0	0.2	33.7	0.0	0.2	19.6	1.57	2.53

The oxide forms and the trace elements Th and U were measured using ICP-MS (Actlabs, 2020). The elements Si to O were calculated stoichiometrically from the oxide form.

B. Petrographic thin sections of sample group (iv)

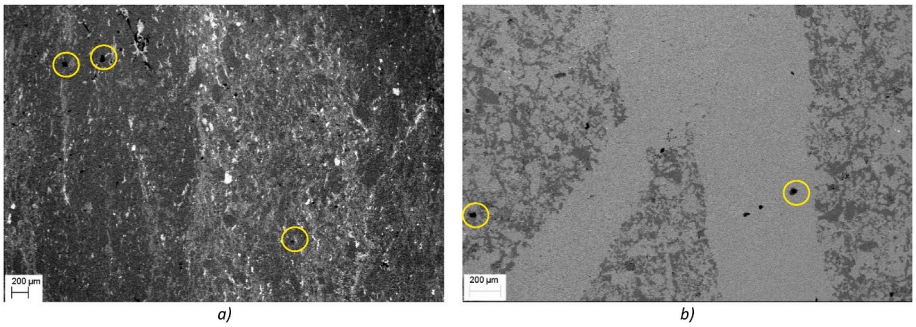

Fig. B-1. Backscattered electron (BSE) images of petrographic thin sections of a) the gneiss pebble and b) the siliceous limestone pebble. The thin section pictures are produced using ZEISS EVO50 scanning electron microscopy (SEM).

(a) The gneiss pebble consists of quartz and feldspars (dark grey), different micas (intermediate grey values) as well as oxides/hydroxides (rare bright spots). Some pores (black spots highlighted by the yellow circles) are visible at the micrometer scale. The elongated quartz and feldspars interlayered by micas form gneissic textures. (b) The siliceous limestone consists of a mixture of quartz and calcite. Veins are frequent (bright bands are pure calcite in the image). Calcite is estimated to represent ~65% of the rock composition, thereby explaining the relatively high ^{37}Ar activity produced (P_{37} = 20.4 Bq). The remaining 35% mainly consists of quartz (SiO_2 = dark grey areas in the BSE image). The black areas (circled in yellow) represent isolated pores on scales of 10–30 μm. Diffusive transport, as observed in the pebbles, was reported to take place at the nanometer scale (Rama and Moore, 1984). Such small pores are not visible in these pictures.

E. Mass dependent production

A set of samples from group (i), ranging in mass between 2.7 g and 8 g, were simultaneously irradiated in pure quartz tubes with the same neutron fluence. The released atoms, without any heating, were collected and the activities were measured. These data revealed a linear relationship between the sample mass and activity (Fig. E-1). The regression line indicates an activity release of 0.5 mBq/g_{CaCO3}. The intersection with the y-axis corresponds to the tank argon activity (6.5×10^{-7} mBq in a 50 cm^3 counter filled at 10 bars). Compared to the activities produced during irradiation, this is regarded as zero.

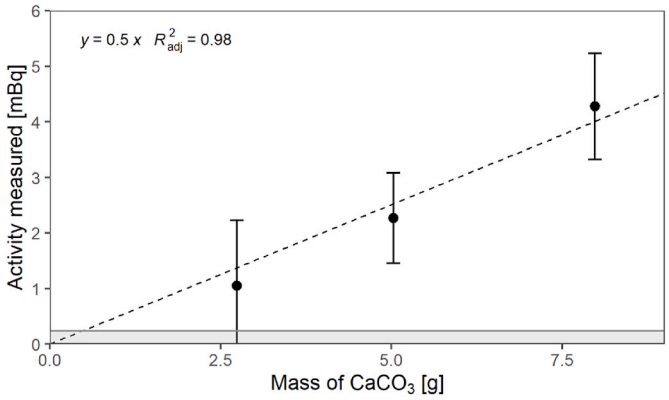

Fig. E-1. Relationship between the irradiated $CaCO_3$ mass [g] and the gross activity measured [mBq]. The shaded area indicates the average minimum detection activity (MDA) for the $CaCO_3$ samples (0.24 mBq). The dashed line is the linear least squares regression model fitted to the data..

C. Cross-control experiment between irradiation containers

For an evaluation of the reproducibility several aliquots of the sediment powder samples (core P54-2), were repeatedly irradiated in alloy vessels (Table C-1, Fig. C-1). y. In addition, results of different types of irradiation vessels were compared. The obtained emanation values all agreed within the range of uncertainties demonstrating the equivalence of different containers. The average emanation in the stainless steel vessels was 2.0 (±0.8)%. This is consistent with the emanation observed from the quartz tube irradiation of 2.4 (±0.3)%.

Table C-1
Results for multiple measurements of sample P54-2.

Container	Run	n_f [cm^{-2}] × 10^{11}	P_{37}[Bq]			A_{gross} [mBq]			BG_{ext}[mBq]			A_{net}[mBq]			ε_T[%]		
Alloy	2	3.9	1.5	±	0.1	61	±	10	11	±	4	51	±	14	3.3	±	1.3
Alloy	3	19.6	6.9	±	0.4	173	±	7	53	±	19	119	±	26	1.7	±	0.6
Alloy	3	19.6	7.1	±	0.4	177	±	9	53	±	19	124	±	27	1.7	±	0.6
Quartz Tube	7	6.9	1.5	±	0.1	37	±	2	0.2	±	1.0	36	±	2	2.4	±	0.3

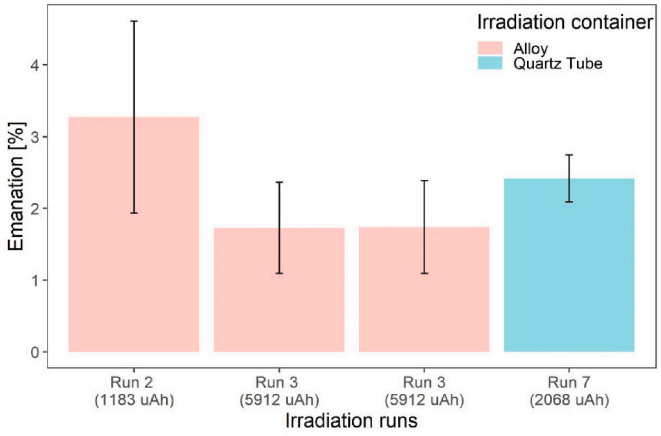

Fig. C-1. Emanation fractions for different irradiation runs and container types.

D. Symbols and units of the parameters used in the equations

Table D-1

Symbol	Unit	Parameter
P_{37}	$atoms\ s^{-1} = Bq$	^{37}Ar production rate or produced activity
N_{tg}	$atoms$	Number of atoms of the target nuclide
$\sigma(E)$	$barns = 10^{-24}\ cm^2$	Energy-dependent cross section
$\dot{\Phi}(E)$	$n\ cm^{-2}\ s^{-1}\ eV^{-1}$	Neutron flux
ε_T	%	Total emanation fraction
ε_D	%	Diffusion emanation fraction (in pore space)
ε_R	%	Recoil emanation fraction
r_0	m	Spherical grain radius
R	m	Recoil range
L	m	Diffusion length
D_{eff}	$m^2\ s^{-1}$	Effective diffusion coefficient in the pore space
ε_{D_s}	%	Solid diffusion emanation fraction
D_s	$m^2\ s^{-1}$	Diffusion coefficient in crystal lattice
λ	s^{-1}	Radioactive constant for ^{37}Ar: $\lambda = 2.3 \times 10^{-7} s^{-1}$
A_T, A_{D_s}, A_R	Bq	Activities emanated: total, by solid diffusive emanation, by recoil
E_a	$kJ\ mol^{-1}$	Activation energy

References

Aalseth, C.E., Day, A.R., Haas, D.A., Hoppe, E.W., Hyronimus, B.J., Keillor, M.E., Mace, E.K., Orrell, J.L., Seifert, A., Woods, V.T., 2011. Measurement of 37Ar to support technology for on-site inspection under the comprehensive nuclear-test-BanTreaty. Nucl. Instrum. Methods Phys. Res. Sect. A Accel. Spectrom. Detect. Assoc. Equip. 652, 58–61. https://doi.org/10.1016/j.nima.2010.09.135.

Actlabs, 2020. Sample Preparation (RX1) and Lithogeochemistry (4Litho).

Adler, P.M., Perrier, F., 2009. Radon emanation in partially saturated porous media. Transport Porous Media 78, 149–159. https://doi.org/10.1007/s11242-008-9291-z.

Alfimov, V., Ivy-Ochs, S., 2009. How well do we understand production of 36Cl in limestone and dolomite? Quat. Geochronol. 4, 462–474. https://doi.org/10.1016/j.quageo.2009.08.005.

Andrews, J.N., Florkowski, T., Lehmann, B.E., Loosli, H.H., 1991. Underground production of radionuclides in the milk river aquifer, Alberta, Canada. Appl. Geochem. 6, 425–434. https://doi.org/10.1016/0883-2927(91)90042-N.

Auger, M., Braccini, S., Ereditato, A., Häberli, M., Kirillova, E., Nesteruk, K.P., Scampoli, P., 2016. Accelerator and detector physics at the Bern medical cyclotron and its beam transport line. Nukleonika 61, 11–14. https://doi.org/10.1515/nuka-2016-0009.

Blokhin, A.I., Gai, E.V., Ignatyuk, A.V., Koba, I.I., Manokhin, V.N., Pronyaev, V.G., 2016. New Version of Neutron Evaluated Data Library BROND-3.1. Problems of Atomic Science and Technology, Series: Nuclear and Reactor Constants.

Braccini, S., 2016. Compact Medical Cyclotrons and Their Use for Radioisotope Production and Multi-Disciplinary Research 6.

Braccini, S., 2013. Particle Accelerators and Detectors for Medical Diagnostics and Therapy. https://doi.org/10.7892/BORIS.75806.

Braccini, S., Ereditato, A., Scampoli, P., Von Bremen, K., 2011. The New Bern Cyclotron Laboratory for Radioisotope Production and Research. Presented at the Proceedings of IPAC2011, Spain.

Burke, B.C., Heimsath, A.M., Dixon, J.L., Chappell, J., Yoo, K., 2009. Weathering the escarpment: chemical and physical rates and processes, south-eastern Australia. Earth Surf. Process. Landforms 34, 768–785. https://doi.org/10.1002/esp.1764.

Carrigan, C.R., Heinle, R.A., Hudson, G.B., Nitao, J.J., Zucca, J.J., 1996. Trace gas emissions on geological faults as indicators of underground nuclear testing. Nature 382, 528–531. https://doi.org/10.1038/382528a0.

Chau, N.D., Chruściel, E., Prokólski, Ł., 2005. Factors controlling measurements of radon mass exhalation rate. J. Environ. Radioact. 82, 363–369. https://doi.org/10.1016/j.jenvrad.2005.02.006.

CUCE, 2007. Cation Exchange Capacity (CEC). (No. #22), Agronomy Fact Sheet Series. Cornell University. Cornell University Cooperative Extension. Department of Crop and Soil Sciences, College of Agriculture and Life Sciences.

Czubek, J.A., 1988. SLOWN2.BAS Program for Calculation of the Rock Neutron Slowing Down Parameters. Institute of Nuclear Physics, Krakow.

Delvaux, B., Herbillon, A.J., Vielvoye, L., 1989. Characterization of a weathering sequence of soils derived from volcanic ash in Cameroon. Taxonomic, mineralogical and agronomic implications. Geoderma 45, 375–388. https://doi.org/10.1016/0016-7061(89)90017-7.

Edmunds, W.M., Darling, W.G., Purtschert, R., Corcho Alvarado, J.A., 2014. Noble gas, CFC and other geochemical evidence for the age and origin of the Bath thermal waters, UK. Appl. Geochem. 40, 155–163. https://doi.org/10.1016/j.apgeochem.2013.10.007.

Fabryka-Martin, J.T., 1988. Production of Radionuclides in the Earth and Their Hydrogeologic Significance, with Emphasis on Chlorine-36 and Iodine-129. University of Arizona.

Fleischer, R.L., 1983. Theory of alpha recoil effects on radon release and isotopic disequilibrium. Geochem. Cosmochim. Acta 47, 779–784. https://doi.org/10.1016/0016-7037(83)90111-4.

Flügge, S., Zimens, K.E., 1939. Die Bestimmung von Korngrößen and von Diffusionskonstanten aus dem Emaniervermögen. Z. Phys. Cherm. B. 42, 179–220.

Forster, M., MOSERl, H., RAMMl, K., Hietel', B., 1989. Investigating the Neutron-Induced Subsurface Production of Environmental Isotopes 37Ar, 39Ar, 3H and 36CI with Neutron Irradiation of Aquifer Material 8.

Guenthner, W.R., Reiners, P.W., Ketcham, R.A., Nasdala, L., Giester, G., 2013. Helium diffusion in natural zircon: radiation damage, anisotropy, and the interpretation of zircon (U-Th)/He thermochronology. Am. J. Sci. 313, 145–198. https://doi.org/10.2475/03.2013.01.

Guillon, S., Sun, Y., Purtschert, R., Raghoo, L., Pili, E., Carrigan, C.R., 2016. Alteration of natural 37Ar activity concentration in the subsurface by gas transport and water infiltration. J. Environ. Radioact. 155 (156), 89–96. https://doi.org/10.1016/j.jenvrad.2016.02.021.

Haas, D.A., Orrell, J.L., Bowyer, T.W., McIntyre, J.I., Miley, H.S., Aalseth, C.E., Hayes, J. C., 2010. The Science Case for 37Ar as a Monitor for Underground Nuclear Explosions (No. PNNL-19458, 992009). https://doi.org/10.2172/992009.

Harrison, T.M., Lovera, O.M., 2014. The multi-diffusion domain model: past, present and future. Geol. Soc. Lond. Special Publ. 378, 91–106. https://doi.org/10.1144/SP378.9.

Heisinger, B., Lal, D., Jull, A.J.T., Kubik, P., Ivy-Ochs, S., Neumaier, S., Knie, K., Lazarev, V., Nolte, E., 2002. Production of selected cosmogenic radionuclides by muons 1. Fast muons. Earth Planet Sci. Lett. 11.

IAEA, 2013. Measurement and Calculation of Radon Releases from NORM Residues, Technical Reports Series/International Atomic Energy Agency. Internat. Atomic Energy Agency, Vienna.

Johnson, C., Armstrong, H., Wilson, W.H., Biegalski, S.R., 2015. Examination of radioargon production by cosmic neutron interactions. J. Environ. Radioact. 140, 123–129. https://doi.org/10.1016/j.jenvrad.2014.10.016.

Johnson, C., Lowrey, J.D., Alexander, T., Mace, E., Prinke, A., 2021. Measurements of the emanation of 37Ar and 39Ar from irradiated rocks and powders. J. Radioanal. Nucl. Chem. 329, 969–974. https://doi.org/10.1007/s10967-021-07827-4.

Johnson, C., Prinke, A., Lowrey, J.D., Humble, P., Mace, E., Alexander, T., Riley, B.J., Williams, R., 2018. A method to quantify the 37Ar emanation fraction in powders and rocks. J. Radioanal. Nucl. Chem. 318, 297–303. https://doi.org/10.1007/s10967-018-6024-9.

Jourdan, F., Matzel, J.P., Renne, P.R., 2007. 39Ar and 37Ar recoil loss during neutron irradiation of sanidine and plagioclase. Geochem. Cosmochim. Acta 18.

Käser, D., Hunkeler, D., 2016. Contribution of alluvial groundwater to the outflow of mountainous catchments. Water Resour. Res. 52, 680–697. https://doi.org/10.1002/2014WR016730.

Krishnaswami, S., Seidemann, D.E., 1988. Comparative study of 222Rn, 40Ar, 39Ar, and 37Ar leakage from rocks and minerals: implications for the role of nanopores in gas transport through natural silicates. Geochem. Cosmochim. Acta.

Lal, D., Peters, B., 1962. Cosmic ray produced isotopes and their application to problems in geophysics. Prog. Elem. Part. Cosmic Ray Phys. 6, 1–74.

Lehmann, B.E., Purtschert, R., 1997. Radioisotope dynamics — the origin and fate of nuclides in groundwater. Appl. Geochem. 12, 727–738. https://doi.org/10.1016/S0883-2927(97)00039-5.

Liu, Chengshuai, Wang, Y., Li, F., Chen, M., Zhai, G., Tao, L., Liu, Chuanping, 2014. Influence of geochemical properties and land-use types on the microbial reduction of Fe(iii) in subtropical soils. Environ. Sci.: Process. Impacts 16, 1938–1947. https://doi.org/10.1039/C4EM00217B.

Loosli, H.H., Lehmann, B.E., Balderer, W., 1989. Argon-39, argon-37 and krypton-85 isotopes in Stripa groundwaters. Geochem. Cosmochim. Acta 53, 1825–1829. https://doi.org/10.1016/0016-7037(89)90303-7.

Loosli, H.H., Purtschert, R., 2005. Rare gases. In: Isotopes in the Water Cycle: Pas, Pressent and Futur of a Developing Science. I.A.E.A, pp. 91–95.

Maraziotis, E.A., 1996. Effects of intraparticle porosity on the radon emanation coefficient. Environ. Sci. Technol. 30, 2441–2448. https://doi.org/10.1021/es950386r.

Morawska, L., Phillips, C.R., 1992. Dependence of the radon emanation coefficient on radium distribution and internal structure ef the material. Geochem. Cosmochim. Acta.

Musy, S., Meyzonnat, G., Barbecot, F., Hunkeler, D., Sültenfuss, J., Solomon, D.K., Purtschert, R., 2021. In-situ sampling for krypton-85 groundwater dating. J. Hydrol. X 11, 100075. https://doi.org/10.1016/j.hydroa.2021.100075.

Onstott, T.C., Miller, M.L., Ewing, R.C., Arnold, G.W., Walsh, D.S., 1995. Recoil refinements: implications for the 40Ar/39Ar dating technique. Geochem. Cosmochim. Acta 59, 1821–1834. https://doi.org/10.1016/0016-7037(95)00085-E.

Paine, J.H., Nomade, S., Renne, P.R., 2006. Quantification of 39Ar recoil ejection from GA1550 biotite during neutron irradiation as a function of grain dimensions. Geochem. Cosmochim. Acta 70, 1507–1517. https://doi.org/10.1016/j.gca.2005.11.012.

Pearson, F.J., Balderer, W., Loosli, H.H., Lehmann, B.E., Matter, A., Peters, Tj, Schmassmann, H., Gautschi, A., 1991. Applied Isotope Hydrogeology: A Case Study in Northern Switzerland (Nagra Technical Report No. NTB 88-01). Nagra.

Peel, M., Kipfer, R., Hunkeler, D., Brunner, P., 2022. Variable 222Rn emanation rates in an alluvial aquifer: limits on using 222Rn as a tracer of surface water – groundwater interactions. Chem. Geol., 120829 https://doi.org/10.1016/j.chemgeo.2022.120829.

Peng, S., Hu, Q., Hamamoto, S., 2012. Diffusivity of rocks: gas diffusion measurements and correlation to porosity and pore size distribution: GAS diffusion and rock porosity and pore size. Water Resour. Res. 48 https://doi.org/10.1029/2011WR011098.

Pola, A., Rastelli, D., Treccani, M., Pasquato, S., Bortot, D., 2020. DIAMON: a portable, real-time and direction-aware neutron spectrometer for field characterization and dosimetry. Nucl. Instrum. Methods Phys. Res. Sect. A Accel. Spectrom. Detect. Assoc. Equip. 969, 164078 https://doi.org/10.1016/j.nima.2020.164078.

Price, J.R., Velbel, M.A., 2003. Chemical weathering indices applied to weathering profiles developed on heterogeneous felsic metamorphic parent rocks. Chem. Geol. 202, 397–416. https://doi.org/10.1016/j.chemgeo.2002.11.001.

Purtschert, R., 2017. Ar-37, Be-7, and Xe-133 in the Atmosphere.

Purtschert, R., 2012. Ar-39 dating of groundwater: how limiting is underground production? Goldschmidt 2012 Conference Abstracts. Mineral. Mag. 76, 1401–2639. https://doi.org/10.1180/S0026461X00008434.

Radulov, I., Berbecea, A., Sala, F., Crista, F., Lato, A., 2011. Mineral Fertilization Influence on Soil pH, Cationic Exchange Capacity, and Nutrient Content 6.

Rama, Moore, W.S., 1984. Mechanism of transport of U-Th series radioisotopes from solids into ground water. Geochem. Cosmochim. Acta 48, 395–399. https://doi.org/10.1016/0016-7037(84)90261-8.

Renne, P.R., Norman, E.B., 2001. Determination of the half-life of 37 Ar by mass spectrometry. Phys. Rev. C 63, 047302. https://doi.org/10.1103/PhysRevC.63.047302.

Riedmann, R.A., Purtschert, R., 2011. Natural argon-37 concentrations in soil air: implications for monitoring underground nuclear explosions. Environ. Sci. Technol. 45, 8656–8664. https://doi.org/10.1021/es201192u.

Rousset, B., 2006. Pierre Jaune de Neuchâtel; Rapport final (No. EC/BR/02601-03). Service de la Protection des Monuments et des Sites, Lausanne.

Sakoda, A., Ishimori, Y., 2017. Mechanisms and modeling approaches of radon emanation for natural materials. Jpn. J. Health Phys. 52, 296–306. https://doi.org/10.5453/jhps.52.296.

Saldanha, R., Back, H.O., Tsang, R.H.M., Alexander, T., Elliott, S.R., Ferrara, S., Mace, E., Overman, C., Zalavadia, M., 2019. Cosmogenic production of Ar 39 and Ar 37 in argon. Phys. Rev. C 100, 024608. https://doi.org/10.1103/PhysRevC.100.024608.

Schaller, M., von Blanckenburg, F., Veldkamp, A., Tebbens, L.A., Hovius, N., Kubik, P.W., 2002. A 30 000 yr record of erosion rates from cosmogenic 10Be in Middle European river terraces. Earth Planet Sci. Lett. 204, 307–320. https://doi.org/10.1016/S0012-821X(02)00951-2.

Schilling, O.S., Gerber, C., Partington, D.J., Purtschert, R., Brennwald, M.S., Kipfer, R., Hunkeler, D., Brunner, P., 2017. Advancing physically-based flow simulations of alluvial systems through atmospheric noble gases and the novel argon-37 tracer method: integrating tracers with models. Water Resour. Res. 53 https://doi.org/10.1002/2017WR020754.

Schwarz, W., 2001. Argon-Geochemie von Mineralen hydrothermaler Bildung (Zeolithe; Serizite in Plagioklas) (PhD). Ruprecht-Karls-Universitaet, Heidelberg.

Semkow, T.M., 1990. Recoil-emanation theory applied to radon release from mineral grains. Geochem. Cosmochim. Acta 54, 425–440. https://doi.org/10.1016/0016-7037(90)90331-E.

Soetaert, K., Meysman, F., 2012. Reactive transport in aquatic ecosystems: rapid model prototyping in the open source software R. Environ. Model. Software 32, 49–60. https://doi.org/10.1016/j.envsoft.2011.08.011.

Solomon, D.K., Hunt, A., Poreda, R.J., 1996. Source of radiogenic helium 4 in shallow aquifers: implications for dating young groundwater. Water Resour. Res. 32, 1805–1813. https://doi.org/10.1029/96WR00600.

Spannagel, G., Fireman, E.L., 1972. Stopping rate of negative cosmic-ray muons near sea level. J. Geophys. Res. 77, 5351–5359. https://doi.org/10.1029/JA077i028p05351.

Šrámek, O., Stevens, L., McDonough, W.F., Mukhopadhyay, S., Peterson, R.J., 2017. Subterranean production of neutrons, 39 Ar and 21 Ne: rates and uncertainties. Geochem. Cosmochim. Acta 196, 370–387. https://doi.org/10.1016/j.gca.2016.09.040.

Strasser, A., Charollais, J., Conrad, M.A., Clavel, B., Pictet, A., Mastrangelo, B., 2016. The Cretaceous of the Swiss Jura Mountains: an improved lithostratigraphic scheme. Swiss J. Geosci. 109, 201–220. https://doi.org/10.1007/s00015-016-0215-6.

Sun, H., Furbish, D.J., 1995. Moisture content effect on radon emanation in porous media. J. Contam. Hydrol. 18, 239–255. https://doi.org/10.1016/0169-7722(95)00002-D.

Suther, B.E., Leigh, D.S., West, L.T., 2021. Soil chemistry and clay mineralogy of an alluvial chronosequence from the North Carolina sandhills of the upper coastal plain, USA. Soil Systems 6, 1. https://doi.org/10.3390/soilsystems6010001.

Watson, E.B., Cherniak, D.J., 2003. Lattice diffusion of Ar in quartz, with constraints on Ar solubility and evidence of nanopores. Geochem. Cosmochim. Acta 67, 2043–2062. https://doi.org/10.1016/S0016-7037(02)01340-6.

Wilson, W.H., Biegalski, S.R., 2015. Evaluating the feasibility of a simple experiment to validate the existence of a low-energy component to the 40Ca(n,α)37Ar reaction cross-section. Isotopes and radiation: general. In: American Nucelar Society Annual Meeting. Presented at the Nuclear Technology: an Essential Part of the Solution, San Antonio, Texas.

Yokochi, R., Sturchio, N.C., Purtschert, R., 2012. Determination of crustal fluid residence times using nucleogenic 39Ar. Geochem. Cosmochim. Acta 88, 19–26. https://doi.org/10.1016/j.gca.2012.04.034.